We therefore accept, provisionally, that these major dust events provide a common stratigraphic marker which allows the direct correlation of the marine and Vostok records. For this purpose, we selected major events recognizable in both records (Fig. 2) that correspond either to maximum values (events 2, 3, 6 and 7) or to the beginning (event 4) or termination (events 1 and 5) of a peak.

To test the validity and limits of this approach we first examine the last climatic transition. Low dust contents at Vostok (Fig. 2*b*) occur at mid-transition (12.2 kyr BP) whereas at RC11-120 (Fig. 2*c*) the minimum in the magnetic susceptibility record occurs about 3.5 kyr later. So large a difference for such a recent event may be explained only partially by dating inaccuracy, either on Vostok or RC11-120; hence we consider this value as a limit of the accuracy of our stratigraphic approach.

Discrepancies between the Vostok core and marine core chronologies before 110 kyr BP have already been noted and discussed[3]. They are due to the different duration of the last interglacial period, which was about twice as long in the Vostok chronology (stage G) as it is in the marine chronology. As a result, at mid-transition from glacial to interglacial (H/G or 6/5), the Vostok temperature leads the global ice volume (as given by the $\delta^{18}O$ SPECMAP record) and the surface temperature at RC11-120 by respectively 10 and 7 kyr (ref. 3). For this transition the time difference between the end of the dust peak (Fig. 2*b*) and the end of the magnetic 'flux' peak is ~10 kyr and using this level as a time marker would put the Vostok temperature record practically in phase with the marine $\delta^{18}O$ record (Fig. 2). The Vostok temperature would then lag the RC11-120 sea surface temperature by ~3 kyr, but this value is not significant given the limit of accuracy mentioned above. Within this limit, we conclude that there was no significant phase shift between the Vostok temperature and the marine records during the previous glacial–interglacial transition. We also note that the time interval between levels 4 and 5 is 30% less in the Vostok than in the marine chronology (from 138 to 66 kyr BP and from 128 to 73 kyr BP respectively). This might reduce the discrepancy between the duration of the last interglacial in the two records, but we note that the 'dust' event during marine stage 4 is less well characterized than those of stages 2 or 6.

Our approach is independent of absolute dating. We note, however, that recent results obtained on coral-reef terraces place the peak of the last interglacial around 126 kyr BP (E. Bard, B. Hamelin, Y. Lao, R. F. Anderson and R. G. Fairbanks, unpublished results) confirming the deep-sea-core dating obtained by orbital tuning[29]. The Vostok timescale would thus be in error. This would be a strong argument against the evidence from a continental sequence[32] for a much earlier interglacial period.

Our stratigraphic approach relies on the critical assumption that magnetic susceptibility in RC11-120 reflects the aeolian input. Our results must be confirmed and all the information relevant to the Vostok and marine chronologies combined before a revised Vostok timescale may be established. We intend to make further magnetic measurements and mineralogical investigations to ascertain the origin of the magnetic material and to extend the technique of using dust as a stratigraphic marker. □

Received 29 June; accepted 8 November 1989.

1. Lorius, C. *et al. Nature* **316,** 591–596 (1985).
2. De Angelis, M., Barkov, N. I. & Petrov, V. N. *Nature* **325,** 318–321 (1987).
3. Jouzel, J. *et al. Nature* **329,** 403–408 (1987).
4. Barnola, J. M., Raynaud, D., Korotkevitch, Y. S. & Lorius, C. *Nature* **329,** 408–414 (1987).
5. Legrand, M., Lorius, C., Barkov, N. I. & Petrov, V. N. *Atmos. Envir.* **22,** 317–331 (1988).
6. Raynaud, D., Chappellaz, J., Barnola, J. M., Korotkevitch, Y. S. & Lorius, C. *Nature* **333,** 655–657 (1988).
7. Legrand, M., Delmas, R. J. & Charlson, R. J. *Nature* **334,** 418–420 (1988).
8. Beget, J. E. & Hawkins, O. B. *Nature* **337,** 151–153 (1989).
9. Kent, D. V. *Nature* **299,** 538–539 (1982).
10. Mounier, L. thesis, Université Scientifique Technologique et Médicale de Grénoble (1988).
11. De Angelis, M. *et al. Atmos. Chem.* **1,** 215–239 (1984).
12. Lorius, C., Raisbeck G., Jouzel, J. & Raynaud D. in *The Environmental Record in Glaciers and Ice Sheets* (eds Oeschger, H & Langway, C. C. Jr) 343–361 (Wiley, Chichester, 1989).
13. Briat, M., Royer, A., Petit, J. R. & Lorius, C. *Ann. Glaciol.* **3,** 27–31 (1982).
14. Gaudichet, A., Petit, J. R., Lefevre, R. & Lorius, C. *Tellus* B**38,** 250–261 (1986).
15. Gaudichet, A. *et al. Geophys. Res. Lett.* **15,** 1471–1474 (1988).
16. Petit, J. R., Briat, M. & Royer, A. *Nature* **293,** 391–394 (1981).
17. Lorius, C., Raynaud, D., Petit, J. R., Jouzel, J. & Merlivat, L. *Ann. Glaciol.* **5,** 88–95 (1984).
18. Guiot, J., Pons A., De Beaulieu, J. L. & Reille, M. *Nature* **338,** 309–313 (1989).
19. Thomson, D. J. *Proc. IEEE* **70,** 1055–1096 (1982).
20. Yiou, F. *et al.* in *Interaction of the Global Carbon Cycle and Climate System, Electric Power Res. Inst. Rep.* (ed. Keir P.) (Kluwer, in the press).
21. Berger, A. I. *J. Atmos. Sci.* **35,** 2362–2367 (1978).
22. Thompson, L. G. & Mosley-Thompson, E. *Science* **212,** 812–815 (1981).
23. Hammer, C. *et al. Geophys. Monogr.* **33,** 90–94 (1985).
24. Heusser, C. J. *Quat. Res.* **16,** 293–321 (1981).
25. Bowler, J. M. *Earth Sci. Rev.* **12,** 279–310 (1976).
26. Kukla, G. *Quat. Sci. Rev.* **6,** 191–219 (1987).
27. Robinson, S. G. *Phys. Earth planet. Inter.* **42,** 22–47 (1986).
28. Hovan, S. A., Rea, D. K., Pisias, N. G. & Shackleton, N. J. *Nature* **340,** 296–298 (1989).
29. Martinson, D. G. *et al. Quat. Res.* **27,** 477–482 (1987).
30. Kolla, V., Henderson, L. & Biscaye, P. *Deep Sea Res.* **23,** 949–961 (1976).
31. Kolla, V. & Biscaye, P. *J. sedim. Pedology.* **47,** 642–649 (1977).
32. Winograd, I. J., Barney, J., Zabo, B. J., Coplin, T. B. & Riggs, A. C., Science, **242,** 1275–1280 (1988).

ACKNOWLEDGEMENTS. We thank M. Creseveur, P. Yiou and C. Genthon for the implementation of the MTM, C. Ritz for the age–depth Vostok model, and M. Ghil, F. Grousset, J. Imbrie, D. Kent, D. Raynaud and W. Ruddiman for discussions.

The role of strain energy in creep graphitization of anthracite

J. V. Ross & R. M. Bustin

Department of Geological Sciences, The University of British Columbia, Vancouver, Canada, V6T 2B4

RECENT research on ceramics and natural minerals has demonstrated that non-hydrostatic stress can affect some polymorphic transitions and can increase reaction rates[1,2]. One such example is the graphitization of anthracite. Under natural conditions graphite forms at temperatures of 300–500 °C and confining pressures of ~500 MPa (refs 3–9). But in simple heating experiments at ambient pressure and high confining pressure (up to 1 GPa), temperatures of ~2,000 °C are required for graphite formation[10–13]. Here we report creep experiments on natural anthracite at temperatures of 300–600 °C, using variable strains and strain rates and a constant confining pressure of 500 MPa. The experiments yield an apparent activation energy of 68.6 kJ mol^{-1} for the steady-state process(es) leading to graphite formation. This value is in marked contrast with simple heating experiments, which require an activation energy of 1,000 kJ mol^{-1} (ref. 10). We suggest that in our experiments, and also under natural conditions, graphitization is facilitated by available strain energy associated with non-hydrostatic stress; such stresses typify conditions of natural graphitization.

Naturally occurring graphite has been documented from many localities (usually under conditions of synkinematic metamorphism associated with high strain) ranging from upper greenschist facies to lower amphibolite facies and above[3–7]. To test the hypothesis that the strain-energy component of natural deformation is a very important part of the energy required for natural graphitization we planned a series of axial-symmetric deformation experiments on natural samples of vacuum-dried anthracite, which were maintained at 110 °C for a minimum of 1 week. These experiments were conducted under reducing conditions, comparable to deformation and metamorphism under natural conditions: methane was evolved during the experiments. We used two types of confining-pressure medium—a solid medium (NaCl) for high-strain experiments (>15% axial shortening)[14] and argon gas for low-strain experiments[15]. All tests were conducted in compression using a confining pressure of 500 MPa, a temperature range of 350–600 °C and constant strain rates of

$1.3\times10^{-6}\,s^{-1}$ to $1.3\times10^{-4}\,s^{-1}$. After being corrected for apparatus and jacket effects[16,18], all stress–strain curves have similar geometry, with the stress difference at any strain decreasing with increasing temperature or with decreasing strain rate; steady-state conditions were achieved at ~5% axial strain. Values of stress difference, measured at 10% axial strain, for different strain rates are shown in Table 1 and are plotted as log (stress difference) against −log (strain rate) in Fig. 1. We use a linear least-squares minimization procedure[16] to fit the data to a power-law creep equation of the form[15]

$$\ln \dot{\varepsilon} = \ln A - Q/RT + n \ln \sigma$$

where A is the pre-exponential factor, Q is the apparent activation energy, n is the stress exponent, $\dot{\varepsilon}$ is the strain rate, T is the temperature (K) and σ is the stress. The best-fit (correlation coefficient, $r=0.92$) isotherms through the data points have a slope n and increase their spacing slightly towards the lower temperatures. The parameters of this fit (confining pressure of 500 MPa) are $A=10^{0.99\pm0.15}\,s^{-1}\ MPa^{-n}\ K$, $Q=68.6\pm1.2$ kJ mol^{-1} and $n=3.3\pm0.2$, where the errors quoted are ±2 standard deviations (95% confidence limits).

We have examined all of the deformed samples and undeformed specimens using reflected light. As previously discussed[19], the maximum reflectance increases with increasing strain and at about 23% strain is preferentially developed parallel to the plane of flattening (plane perpendicular to the maximum compressive stress, or load axis); and the bireflectance (the difference between maximum and minimum reflectance) increases.

Reordering of the molecular structure accompanying deformation suggested by optical property(s) is also evident in transmission electron microscopy (TEM) of the undeformed and deformed samples. Undeformed samples are characterized by elongated (10–20-nm) pores lying in the bedding plane and by pore walls composed of 'stacks' of basic structural units (BSUs) or aromatic layers that are 1–5 nm thick and up to 10 nm long (Fig. 2). These configurations are similar to those previously described[6,13]. Using TEM we examined two samples that were shortened by >25% at 600 °C using a strain rate of $10^{-5}\,s^{-1}$, and found them to be heterogeneous in structure. The pore size (5–10 nm in length) and density were reduced and the BSUs were preferentially oriented in the plane of flattening. The BSUs of which the pore walls were composed, although turbostratic[3], had a more planar or linear nature in the flattening plane.

TABLE 1 Stress difference at various strain rates

Temperature °C	Strain rate $10^{-4}\,s^{-1}$	$10^{-5}\,s^{-1}$	$10^{-6}\,s^{-1}$
350	660	354	177
400	478	220	135
450	398	186	95
500	316	162	81
550	269	131	66
600	213	107	52

Stress difference ($\sigma_3-\sigma_1$) (in MPa) measured at 10% axial strain in experiments at a constant confining pressure of 500 MPa.

Selected-area diffraction (SAD) imaging in the dark field shows many microstructural orientations within the specimen (Fig. 3*a*). Other areas show strong preferred orientation in SAD images of their (002) lattice fringes (Fig. 3*b*), indicating that a high degree of anisotropy is associated with strains of over 23%, similar to the structure of graphite produced at high temperature and ambient pressure by simple heating. At some positions, where the anisotropy seems to be greatest, dark-field imaging shows a crystalline SAD pattern (Fig. 3*c*) and the bright-field images are characterized by Bragg and Moiré fringes (Fig. 3*d*), indicative of graphite lamellae that may be either single crystals or overlapping crystallites.

TEM of undeformed and deformed specimens gives insight into the process(es) operating during steady-state deformation: that results in the formation of graphite. Pores have coalesced, rotated and become aligned in the flattening plane of the experiments. Furthermore, the BSUs or stacks of aromatic layers have become more ordered, with the eventual production of graphite. This long-range ordering of the structure(s) is associated with large values of reflectivity and bireflectance of highly strained samples. The graphite produced in the deformation experiments is comparable to that produced by simple heating under ambient pressure. We suggest that the activation energy of 1,000 kJ mol^{-1} associated with simple heating experiments is the sum of the thermal activation energy 68.6 kJ mol^{-1} for diffusion-biased creep[17] and the strain energy imparted to the sample(s) during a minimum of 23% axial shortening.

Recent reviews[20] show that most solid-state transformations involve nucleation and growth and, with a suitable driving stress,

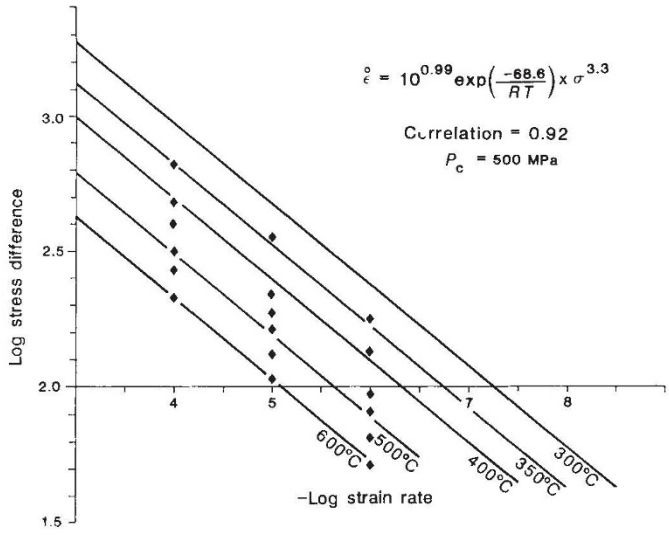

FIG. 1 The logarithm of stress difference plotted against the logarithm of the strain rate for steady-state data from constant-strain-rate, constant-temperature experiments (data shown in Table 1). All experiments at 500-MPa confining pressure and stress difference measured at 10% strain.

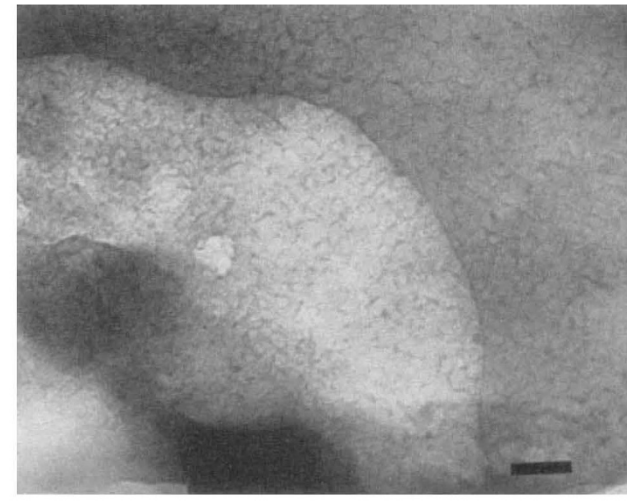

FIG. 2 Transmission electron micrograph (dark field) of the starting material (undeformed specimen of anthracite), showing the network of (002) images indicating the microporosity and sections of the aromatic layers or BSUs of which the pore walls are composed. Scale bar is 1,000 nm.

can occur at low temperatures requiring little thermal activation. These transformations therefore occur by the well-known effect of shear stress on reaction kinetics observed in many ceramics and minerals[21-23]. In natural deformation the production of graphite at the much lower temperatures of 400–500 °C is probably aided by shear-strain effects accompanying natural deformation. In nature, shear strains are often in excess of $\gamma = 2$ ($\gamma = 2$ corresponds to axial shortening of ~60%). This process of graphite formation is also probably related to the diffusional release of H^+ and CH_4 molecules associated with structural rearrangement and alignment of BSUs. The rest of the activation energy needed for the graphitization process comes from shear strain, which facilitates the straightening of the aromatic layers to a more uniform graphite packing and, on the scale of the optical microscope, also leads to an increase in reflectivity and bireflectance. □

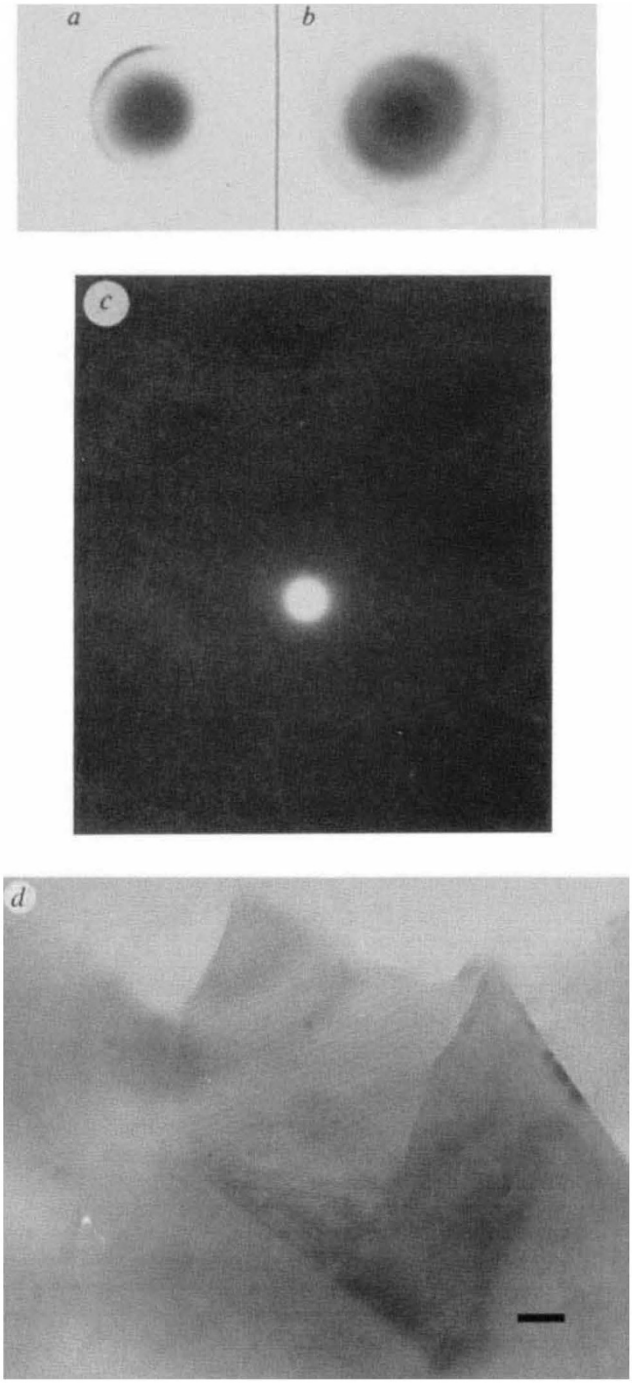

FIG. 3 *a*, Selected-area diffraction pattern (SAD—dark field) of highly deformed specimen, showing (002) ring containing 'spotty' reflections, indicating that the layers are turbostratic. *b*, SAD (dark-field) pattern from same specimen showing well developed arcuate pattern of the (002) ring, indicating a high degree of preferred orientation of the aromatic layers. *c*, Dark-field SAD pattern of crystalline graphite. *d*, Bright-field electron micrograph of region in *c*, showing graphite lamellae having 0.335-nm spacing, with Bragg fringes and poorly developed Moiré fringes, resulting from partial overlapping and rotation of graphite lamellae. Scale bar is 10 nm.

Received 31 July; accepted 10 November 1989.

1. Poirier, J.-P. *Creep of crystals* (Cambridge University Press, London, 1985).
2. Snow, E. & Yund, R. A. *J. metamorphic Geol.* **5**, 141–153 (1987).
3. Franklin, R. E. *Proc. R. Soc.* **209**, 196–218 (1951).
4. Evans, E. L., Jenkins, J. L. & Thomas, J. M. *Carbon* **10**, 637–642 (1972).
5. Diessel, C. F. K., Brothers, R. N. & Black, P. M. *Contr. Miner. Petrol.* **68**, 63–78 (1978).
6. Deurbergue, A., Oberlin, A., Oh, J.-H. & Rouzaud, J. N. *Int. J. Coal Geol.* **8**, 375–393 (1987).
7. Oh, J.-H. thesis, Univ. d'Orléans (1987).
8. Landis, C. A. *Contr. Miner. Petrol.* **30**, 34–45 (1971).
9. Okuyama-Kusunose, Y. & Itaya, T. *J. metamorphic Geol.* **5**, 121–139 (1987).
10. Bonijoly, M., Oberlin, M. & Oberlin, A. *Int. J. Coal Geol.* **1**, 283–313 (1982).
11. Noda, T. & Kato, H. *Carbon* **3**, 289–297 (1965).
12. Oberlin, A. *Carbon* **22**, 521–541 (1984).
13. Rouzaud, J. N. thesis, Univ. Orléans (1984).
14. Green, H. W., Griggs, D. T. & Christie, J. M. in *Experimental and Natural Rock Deformation* (ed. Paulitsch, P.) 272–335 (Springer, New York, 1970).
15. Heard, H. C. *Geol. Soc. Am. Mem.* **79**, 193–244 (1960).
16. Heard, H. C. & Raleigh, C. B. *Geol. Soc. Am. Bull.* **83**, 935–956 (1972).
17. Carter, N. L. *Rev. Geophys. Space Phys.* **14**, 301–360 (1976).
18. Parrish, D. K., Krivz, A. & Carter, N. L. *Tectonophysics* **32**, 183–207 (1976).
19. Bustin, R. M., Ross, J. V. & Moffat, I. *Int. J. Coal Geol.* **6**, 343–351 (1986).
20. Rubie, D. C. & Thompson, A. B. *Adv. phys. Geochem.* **4**, 27–79 (1985).
21. Poirier, J.-P. *J. geophys. Res.* **87**, 6791–6797 (1982).
22. Petrovich, R. *Geochim. cosmochim. Acta* **45**, 1665–1674 (1981).
23. Gillet, P. & Madon, M. *Bull. Miner.* **105**, 590–597 (1982).

Viral mortality of marine bacteria and cyanobacteria

Lita M. Proctor*† & Jed A. Fuhrman‡

* Marine Sciences Research Center, State University of New York at Stony Brook, Stony Brook, New York 11794-5000, USA
‡ Department of Biological Sciences, University of Southern California, Los Angeles, California 90089-0371, USA

DESPITE the importance of cyanobacteria in global primary productivity[1] and of heterotrophic bacteria in the consumption of organic matter in the sea[2], the causes of their mortality, particularly the cyanobacteria, are poorly understood. It is usually assumed that mortality is due to protozoan grazing[3,4] rather than to viral infection, probably because abundances of phage and host in nature are presumed to be low[5]. Previously, either very few marine bacteriophages have been found by plaque assays[6–9], or viruses have been simply observed[10–12] or counted[13,14] by transmission electron microscopy, with the assumption that 'phage-looking' forms are locally active bacteriophages. Here we report not only high viral abundance in the ocean but also counts of bacteria and cyanobacteria in the final irreversible stage of lytic infection. The latter counts are necessary to evaluate mortality, because the sources, hosts, viability and ages of observed free viruses are unknown; even finding viruses attached to cells does not prove successful infection. Up to 7% of the heterotrophic bacteria and 5% of the cyanobacteria from diverse marine locations contained mature phage; interpretation via culture data indicates that up to 70% of the prokaryotes could be infected. These data demonstrate the existence of a significant new pathway of carbon and nitrogen cycling in marine food webs and have further implications for gene transfer between marine organisms.

† Present address: Department of Biological Sciences, University of Southern California, Los Angeles, California 90089-0371, USA.